# Interfacial Modulation with Aluminum Oxide for Efficient Plasmon-Induced Water Oxidation

Zeng, Bin; Wang, Shengyang; Gao, Yuying; Li, Guanna; Tian, Wenming; Meeprasert, Jittima; Li, Hao; Xie, Huichen; Fan, Fengtao; More Authors

**Important note**
To cite this publication, please use the final published version (if applicable).
Please check the document version above.

**FULL PAPER**

ADVANCED
FUNCTIONAL
MATERIALS

www.afm-journal.de

Check for updates

# Interfacial Modulation with Aluminum Oxide for Efficient Plasmon-Induced Water Oxidation

*Bin Zeng, Shengyang Wang, Yuying Gao, Guanna Li, Wenming Tian, Jittima Meeprasert, Hao Li, Huichen Xie, Fengtao Fan, Rengui Li,\* and Can Li\**

Plasmon-induced photocatalysts hold great promise for solar energy conversion owing to their strong light-harvesting ability and tunable optical properties. However, the complex process of interfacial extraction of hot carriers and the roles of metal/semiconductor interfaces in plasmonic photocatalysts are still not clearly understood. Herein, the manipulation of the interface between a plasmon metal (Au) and a semiconductor (rutile $TiO_2$) by introducing an interfacial metal oxide ($Al_2O_3$) is reported. The resulting $Au/Al_2O_3/TiO_2$ exhibits remarkable enhancement in photocatalytic water oxidation activity compared with $Au/TiO_2$, giving an apparent quantum efficiency exceeding 1.3% at 520 nm for photocatalytic water oxidation. Such an interfacial modulation approach significantly prolongs the lifetime of hot carriers in the $Au/TiO_2$ system, which conclusively improves the utilization of hot carriers for plasmon-induced water oxidation reaction upon irradiation. This work emphasizes the essential role of the interfacial structure in plasmonic devices and provides an alternative method for designing efficient plasmonic photocatalysts for solar energy conversion.

## 1. Introduction

Surface plasmon resonance (SPR) of metal nanoparticles has emerged as an attractive topic in the field of photocatalysis

B. Zeng, Dr. S. Wang, Y. Gao, H. Li, H. Xie, Prof. F. Fan,
Prof. R. Li, Prof. C. Li
State Key Laboratory of Catalysis
Dalian Institute of Chemical Physics
Chinese Academy of Sciences
Dalian National Laboratory for Clean Energy
457 Zhongshan Road, Dalian 116023, China
E-mail: rgli@dicp.ac.cn; canli@dicp.ac.cn
B. Zeng, Y. Gao, H. Li, H. Xie
University of Chinese Academy of Sciences
Beijing 100049, China
Dr. G. Li, J. Meeprasert
Inorganic Systems Engineering
Department of Chemical Engineering
Delft University of Technology
Van der Maasweg 9, Delft 2629 HZ, The Netherlands
Dr. W. Tian
State Key Laboratory of Molecular Reaction Dynamics and the Dynamic
Research Center for Energy and Environmental Materials
Dalian Institute of Chemical Physics
Chinese Academy of Sciences
Dalian 116023, China

The ORCID identification number(s) for the author(s) of this article can be found under https://doi.org/10.1002/adfm.202005688.

owing to its merits of high optical extinction coefficient, large scattering cross-section, fast plasmonic energy transfer, and tunable light-harvesting range.[1–8] In a typical plasmonic photocatalyst $Au/TiO_2$, the Schottky barrier formed at the interface between the plasmonic metal and semiconductor could prevent the recombination of plasmon-induced holes and electrons.[9] The processes of photoexcitation and separation of hot carriers proceed via a series of consecutive steps, and a sufficient kinetic energy and momentum for hot carriers transferring across the interface barrier are necessary.[10–12] Furthermore, the hot carriers generated from the SPR decay to drive a chemical reaction are much more complicated, particularly in the photocatalytic water oxidation process.[13–16] Although charge injection from plasmonic metals into semiconductors to induce chemical reactions has been extensively studied, the complex process of interfacial extraction and the short lifetime of hot carriers significantly limit the efficiencies of plasmon-induced chemical reactions.[3,4,8,17–24]

The interfacial structure between plasmonic metals and semiconductors plays a significant role in facilitating the separation of plasmon-induced hot carriers.[25–29] For instance, the interaction between metals and semiconductors can form a hybrid chemical interface to improve the process of SPR excitation and charge transfer.[30] Wu et al. reported that a strong interaction between Au and CdSe with strong SPR damping can generate an interfacial charge-transfer transition to enhance the electron injection efficiency.[21] For representative plasmonic photocatalyst $Au/TiO_2$, we previously demonstrated that the interface between Au nanoparticles and $TiO_2$ mainly provides reactive sites for the hole-involved water oxidation reaction.[14] These studies show the importance of the interfacial structure in plasmonic photocatalysts. However, it is still unclear how the interfacial structure works in plasmon-induced photocatalytic reactions, particularly for the challenging water oxidation reaction.

Herein, using a prototypical $Au/TiO_2$ catalyst, we report a feasible strategy to manipulate the interface between the plasmon metal (Au) and the semiconductor (rutile $TiO_2$) by modifying an interfacial metal oxide ($Al_2O_3$). By introducing interfacial $Al_2O_3$ between Au and $TiO_2$, the spatial separation and extraction of plasmon-induced hot carriers could be greatly boosted, and an apparent quantum efficiency (AQE) above 1.3% of

**Figure 1.** HRSEM images of a) Au/TiO$_2$ and b) Au/Al$_2$O$_3$/TiO$_2$. c) Au size distribution of Au/TiO$_2$ and Au/Al$_2$O$_3$/TiO$_2$. d) UV–vis diffuse reflection spectra of Au/TiO$_2$ and Au/Al$_2$O$_3$/TiO$_2$. HRTEM results showing e) bright-field and f) dark-field images of Au/Al$_2$O$_3$/TiO$_2$.

photocatalytic water oxidation at 520 nm was achieved. The role played by Al$_2$O$_3$ species and the interfacial structure in influencing the long-lived hot carriers in plasmonic photocatalysts was also discussed.

## 2. Results and Discussion

### 2.1. Fabrication and Characterization of Au/Al$_2$O$_3$/TiO$_2$

Al$_2$O$_3$ was introduced on the rutile TiO$_2$ surface using an impregnation process, and Au nanoparticles were then deposited to form Au/Al$_2$O$_3$/TiO$_2$ via a traditional deposition–precipitation method similar to that for Au/TiO$_2$. **Figure 1**a,b depicts the size distribution of Au/TiO$_2$ and Au/Al$_2$O$_3$/TiO$_2$, determined by high-resolution scanning electron microscopy (HRSEM). The average size of the Au nanoparticles on TiO$_2$ was ≈4.0 nm and a slightly increased size of ≈4.6 nm was observed when Al$_2$O$_3$ was deposited on TiO$_2$ (Figure 1c). Inductively coupled plasma analysis indicated that the Au contents in Au/TiO$_2$ and Au/Al$_2$O$_3$/TiO$_2$ were 1.72% and 1.69%, respectively, which is lower than the desired value of 2% (Table S1, Supporting Information). The amount of Au loading onto TiO$_2$ was the same as that with Al$_2$O$_3$ modulation. As shown in Figure 1d, the SPR absorption peak showed a blue shift from 590 to 560 nm after the introduction of Al$_2$O$_3$ between Au and TiO$_2$. The SPR of model spherical plasmonic nanoparticles can be described in a dipolar electric mode, in which the SPR frequency is closely related to the size distribution and surrounding electric environment of the metal.[31] Owing to the lower dielectric constant of Al$_2$O$_3$ (9.35) than that of TiO$_2$ (86), such a blue shift for SPR absorption is a result of the different dielectric properties that induce variations in the surrounding electric environment.

No characteristic diffraction peaks of the Al$_2$O$_3$ phase were observed in the X-ray diffraction (XRD) patterns, confirming the amorphous nature of the Al$_2$O$_3$ formed with 1% Al loading. In addition, Au/Al$_2$O$_3$/TiO$_2$ showed no XRD peaks of Al$_2$O$_3$, even when the pretreatment temperature was increased to 1123 K (Figure S1a, Supporting Information). In addition, small crystalline-phase peaks of Al$_2$O$_3$ appeared at Au/Al$_2$O$_3$/TiO$_2$ with Al$_2$O$_3$ content over 5%, as the amount of Al$_2$O$_3$ exceeded the surface capacity of the TiO$_2$ (Figure S1b, Supporting Information). It is suspected that Al$_2$O$_3$ may form a highly spontaneous dispersion and is amorphous on TiO$_2$. Figure 1e,f shows that amorphous Al$_2$O$_3$ was decorated on the surface of TiO$_2$ with no crystalline or large Al$_2$O$_3$ nanoparticles, as observed by high-resolution transmission electron microscopy (HRTEM). The distribution of Au and Al$_2$O$_3$ was further verified by high-angle annular dark-field (HAADF) scanning transmission electron microscopy (HAADF-STEM) and elemental mapping. The elemental mapping images (**Figure 2**) also demonstrate that no aggregated Al$_2$O$_3$ particles were observed and that the alumina species were evenly distributed on the TiO$_2$ surface.

### 2.2. Plasmon-Induced Photocatalytic Water Oxidation

Plasmon-induced photocatalytic water oxidation was conducted in the presence of Fe(NO$_3$)$_3$ under visible-light irradiation ($\lambda \geq 480$ nm). As the bandgap of TiO$_2$ was measured to be 3.02 eV (Figure S2a, Supporting Information), the obtained photocatalytic water oxidation activity was induced by the SPR effect of the Au nanoparticles. As shown in **Figure 3**a, the Au/Al$_2$O$_3$/TiO$_2$ demonstrated a great enhancement in the plasmon-induced water oxidation activity compared to Au/TiO$_2$,
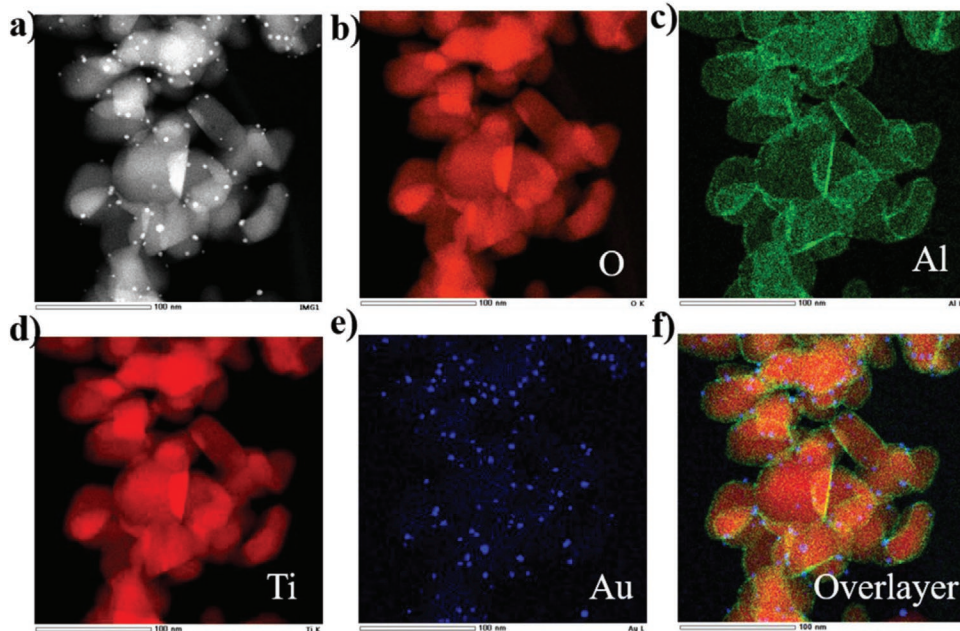
**Figure 2.** a) HAADF-STEM image of Au/Al$_2$O$_3$/TiO$_2$. b–f) Elemental maps of Ti, O, Al, and Au.
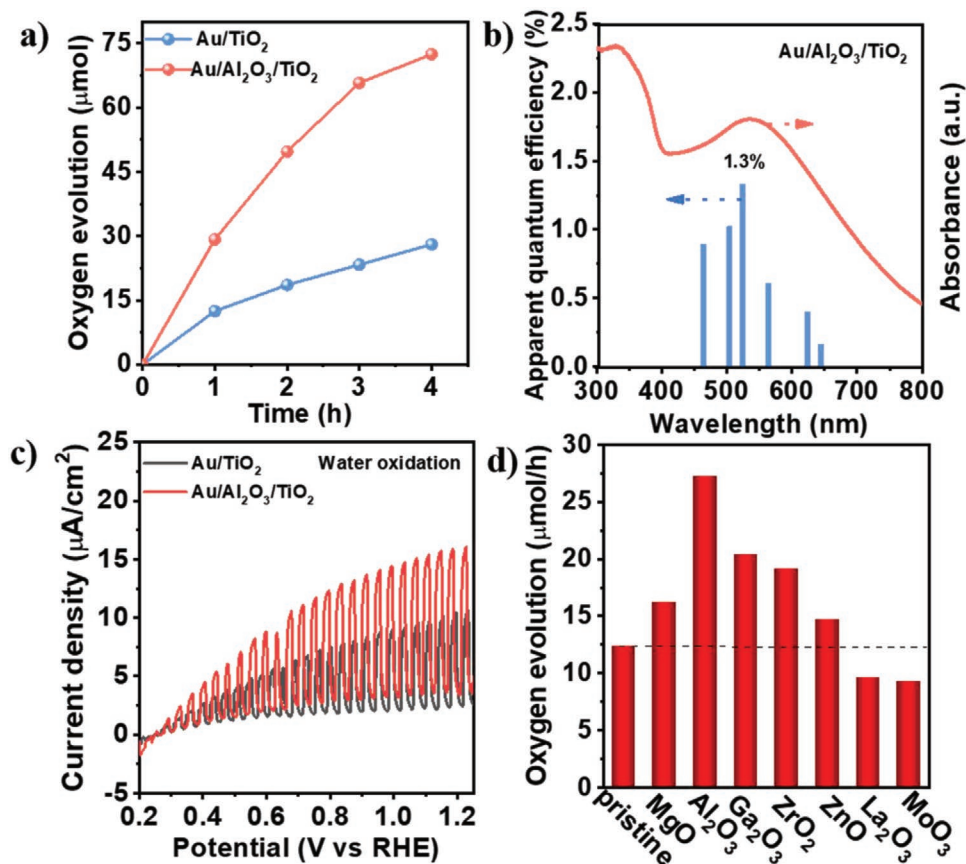


**Figure 3.** a) Time course of photocatalytic oxygen evolution from Au/TiO$_2$ and Au/Al$_2$O$_3$/TiO$_2$. b) Apparent quantum efficiency of Au/Al$_2$O$_3$/TiO$_2$. c) Photoelectrochemical performance of the Au/TiO$_2$ and Au/Al$_2$O$_3$/TiO$_2$ measured in linear sweep voltammetry under 300-W Xe lamp irradiation with 480-nm cutoff filter in NaSO$_4$ aqueous solution. d) Comparison of photocatalytic water oxidation activity of Au/TiO$_2$ with various interfacial metal oxides species modulation; Experiment condition: 50 mg catalyst, 100 mL of 5.0 mM Fe(NO$_3$)$_3$ aqueous solution, light source: Xe lamp (300 W) with Y48 band pass filter ($\lambda \geq 480$ nm), reaction time: 1.0 h.

**ADVANCED
SCIENCE NEWS**

www.advancedsciencenews.com

**ADVANCED
FUNCTIONAL
MATERIALS**

www.afm-journal.de

with the optimal $Au/Al_2O_3/TiO_2$ configuration delivering ≈2.5 times the activity seen with $Au/TiO_2$. As $Fe^{3+}$ ions were used as electron acceptors for water oxidation, the resulted $Fe^{2+}$ ions will also be coexisting in the solution during the photocatalytic reaction and the $Fe^{2+}$ ions are accumulated with reaction proceeding. As a result, the oxidation reverse reaction, that is, the oxidation of $Fe^{2+}$ by photogenerated holes is inevitable in this condition for both $Au/TiO_2$ and $Au/Al_2O_3/TiO_2$, which is similar to the reported literatures.[32,33] The activity slightly decreased as the reaction continued. To evaluate the stability of interfacial $Al_2O_3$ in acid reaction condition, the $Au/Al_2O_3/TiO_2$ was pretreated in 5 M $HNO_3$ solution to simulate long-term acidic condition. After $HNO_3$ treating, the $Au/Al_2O_3/TiO_2$ still shows great enhanced activity compared with $Au/TiO_2$ and comparable activity with pristine $Au/Al_2O_3/TiO_2$ which suggest interfacial $Al_2O_3$ is stable in acid condition (Figure S2b, Supporting Information). Upon further increasing in $Al_2O_3$ content, the water oxidation activity gradually decreased (Figure S3a, Supporting Information). Moreover, the $Au/Al_2O_3/TiO_2$ photocatalyst achieved photocatalytic water oxidation in the range of SPR absorption even at wavelengths longer than 700 nm (Figure S3b, Supporting Information). Figure 3b reveals the measured AQE for photocatalytic water oxidation, which exhibits a trend similar to that of the SPR absorption of Au nanoparticles, demonstrating that the photocatalytic water oxidation activity was driven by the hot carriers induced from SPR of the Au nanoparticles. The optimized AQE of $Au/Al_2O_3/TiO_2$ exceeds 1.3% at 520 nm, which is ≈2.8 times higher than that of $Au/TiO_2$ (0.46%) (Figure S4, Supporting Information). To the best of our knowledge, this is one of the highest AQEs for visible-light-driven water oxidation in plasmonic photocatalysts reported thus far.[24] Meanwhile, linear sweep voltammetry of the photoelectrochemical (PEC) test was performed to evaluate the water oxidation activity in $NaSO_4$ aqueous solution under light chopping conditions. As shown in Figure 3c, the water oxidation photocurrent of $Au/Al_2O_3/TiO_2$ was much higher than that of $Au/TiO_2$, which confirms that the plasmon-induced water oxidation activity is attributed to the hole-involved water oxidation. Furthermore, $Au/Al_2O_3/TiO_2$ shows higher $CH_3OH$ oxidation current than the pristine $Au/TiO_2$. Compared with water oxidation, the photocurrent of the $CH_3OH$ oxidation of $Au/Al_2O_3/TiO_2$ showed an evident enhancement only at low bias voltage, while $Au/TiO_2$ showed enhanced photocurrent in a wider bias range (Figure S5, Supporting Information). These results indicate that the interfacial hot electron extraction is the key step for plasmon-induced water oxidation on $Au/TiO_2$. Furthermore, various interfacial metal oxides (e.g., MgO, $Ga_2O_3$, $ZrO_2$, and ZnO) have also been constructed and proven to contribute enhancements in photocatalytic water oxidation, confirming the universality of interfacial modulation for plasmon-induced photocatalytic reactions (Figure 3d). Anatase and P25 were also chosen as substrates to investigate the phase influence on the interface structure modulation on $Au/TiO_2$. Among all the tested $Au/TiO_2$ configurations, Au/rutile showed the best plasmon-induced water oxidation activity, while the samples with $Al_2O_3$ modulation showed enhanced water oxidation activity regardless of the phase structure (Figure S6, Supporting Information).

## 2.3. Identifying Effects of Interfacial $Al_2O_3$ Species

To accurately identify the effects of interfacial $Al_2O_3$ species, atomic layer deposition (ALD) was employed to precisely control the thickness of the $Al_2O_3$ layer while the Au was loaded onto the substrate by electrostatic adsorption (for details, see the Experimental Section). **Figure 4**a shows that an $Al_2O_3$ layer with a thickness of ≈1.0 nm was formed between Au and $TiO_2$ after ten cycles, and the estimated growth rate of $AlO_x$ was ≈1 Å per cycle. As shown in Figure 4a,b, if Au was separated from $TiO_2$ by 1 nm $Al_2O_3$, it shows no activity. In contrast, the modified sample with an ultrathin (0.2 nm) $Al_2O_3$ layer showed enhanced photocatalytic activity, with the SPR absorption peak located between $Au/TiO_2$ and $Au/Al_2O_3$, indicating that Au nanoparticles (NPs) were located at the interface of $TiO_2/Al_2O_3$ and in contact with both the $Al_2O_3$ and $TiO_2$ (Figure 4c). The structure of $Au/Al_2O_3/TiO_2$ is different from that of a plasmonic metal–insulator–semiconductor in which the metal is isolated by the insulator layer.

$Al_2O_3$ NPs, instead of an ultrathin layer, were introduced to further prove the effect of interfacial $Al_2O_3$ on plasmon-induced water oxidation. In this case, during the deposition of Au nanoparticles, the Au was located either on the surface of the $TiO_2$ and $Al_2O_3$ or at the boundary of $Al_2O_3/TiO_2$. The SPR absorption of $Au/Al_2O_3$ (NP)/$TiO_2$ also showed a blue shift compared to that of $Au/TiO_2$, as shown in Figure 4d. Although some Au nanoparticles were located directly on the surface of $TiO_2$ or $Al_2O_3$, the photocatalytic performance was still enhanced compared with $Au/TiO_2$ (Figure 4e,f). Since $Au/Al_2O_3$ is not active under visible-light irradiation, the interfacial $Al_2O_3$ was proposed to be responsible for the enhanced water oxidation activity. Although surface defect passivation is considered an important effect for enhanced performance in plasmonic systems,[34,35] no oxygen vacancies or $Ti^{3+}$ could be observed in $Au/TiO_2$ or $Au/Al_2O_3/TiO_2$ (Figure S7, Supporting Information). Au nanoparticles were decorated on $TiO_2$ surface following with $Al_2O_3$ modification ($Al_2O_3/Au$-$TiO_2$) and the $TiO_2$ was pretreated under high temperature to passivate the undetectable defects. The resulting $Al_2O_3/Au$–$TiO_2$ displayed a decrease in the photocatalytic activity compared to $Au/TiO_2$ (Figure S8a, Supporting Information). As shown in Figure S8b, Supporting Information, $Au/TiO_2$ did not demonstrate obvious enhancement of the photocatalytic water oxidation activity with increasing annealing temperature, nor did the passivating surface defects give rise to better water oxidation activity. In contrast, $Au/Al_2O_3/TiO_2$ shows greatly enhanced photocatalytic activity compared with $Au/TiO_2$ regardless of the temperature. In conclusion, the effect of $Al_2O_3$ passivation does not contribute to the enhanced plasmon-induced water oxidation.

X-ray photoelectron spectroscopy (XPS) characterizations were conducted to investigate the effect of interfacial $Al_2O_3$ on the interaction between Au and $TiO_2$. As shown in **Figure 5**a, the Al 2p peak at 74.0 eV and the Al–O peak at 531.4 eV confirm the existence of $Al_2O_3$ species.[36] The metallic Au species in both $Au/TiO_2$ and $Au/Al_2O_3/TiO_2$ were verified by the appearance of Au peaks at 83.3 and 83.1 eV. The electron transfer from the support to the metal NPs is a strong indicator of the improved interfacial contact between the Au NPs and $TiO_2$.[37–39] An obvious negative shift in the Au 4f binding energy for
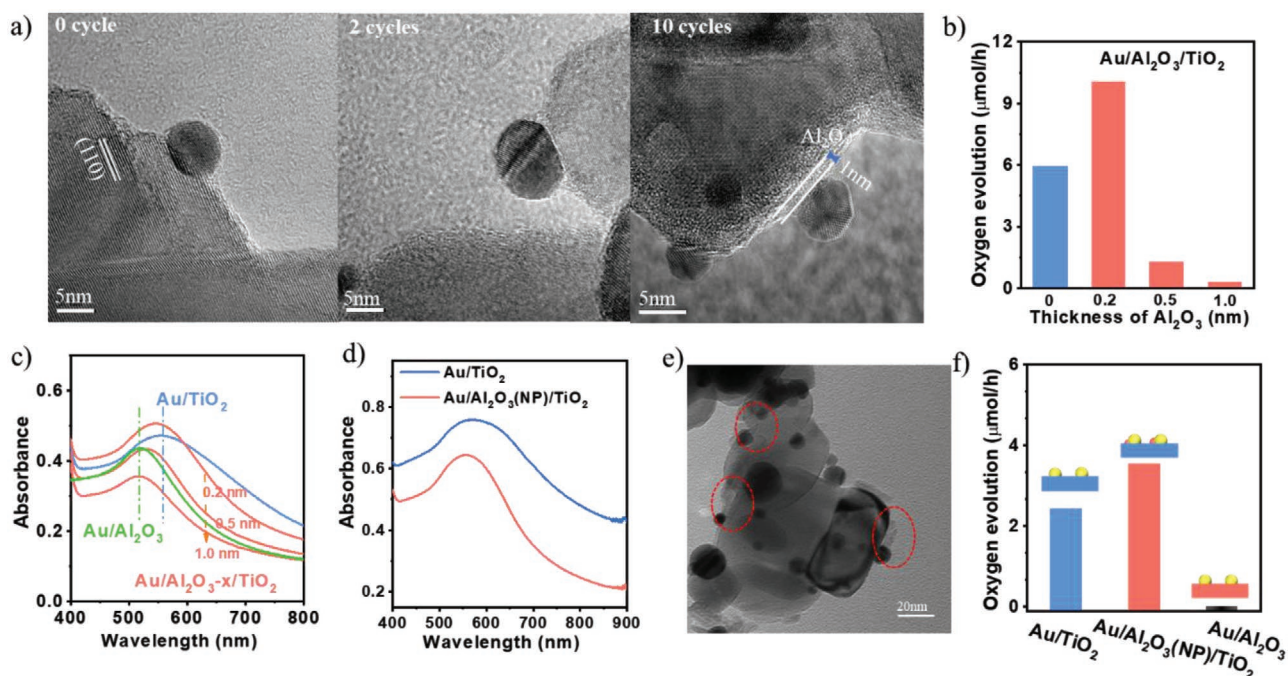
**Figure 4.** a) HRTEM images of $Au/Al_2O_3/TiO_2$ prepared by ALD deposition. b) Photocatalytic water oxidation activity of $Au/Al_2O_3/TiO_2$ with different $Al_2O_3$ ALD cycles. c) UV–vis diffuse reflection spectra of $Au/Al_2O_3/TiO_2$ with different $Al_2O_3$ ALD cycles. d) UV–vis diffuse reflection spectra of $Au/TiO_2$ and $Au/Al_2O_3$ (NP)$/TiO_2$. e) TEM image of $Au/Al_2O_3$ (NP)$/TiO_2$. f) Photocatalytic activity of $Au/TiO_2$ and $Au/Al_2O_3$ (NP)$/TiO_2$.

$Au/Al_2O_3/TiO_2$ implies that the Au and $TiO_2$ interactions were enhanced (Figure 5b). O1s XPS peaks at 529.7 and 530.7 eV are attributed to the lattice oxygen and surface-adsorbed oxygenated species, such as $-OH$ and $H_2O$, respectively.[40] These two O 1s peaks have a blue shift to 530.0 and 531.4 eV in case of $Au/TiO_2$ suggests the electron transfer from $TiO_2$ to Au.

For $Au/Al_2O_3/TiO_2$, the binding energy of lattice oxygen in $Au/Al_2O_3/TiO_2$ (529.7 eV) had a red shift compared with that of $Au/TiO_2$ (530.0 eV) and the more obvious peak at 531.4 eV is related to the coexistence of Al–O and surface-adsorbed oxygenated species,[36] clarifying that $Al_2O_3$ incorporated on the $TiO_2$ surface plays a significant role in enhancing the interfacial
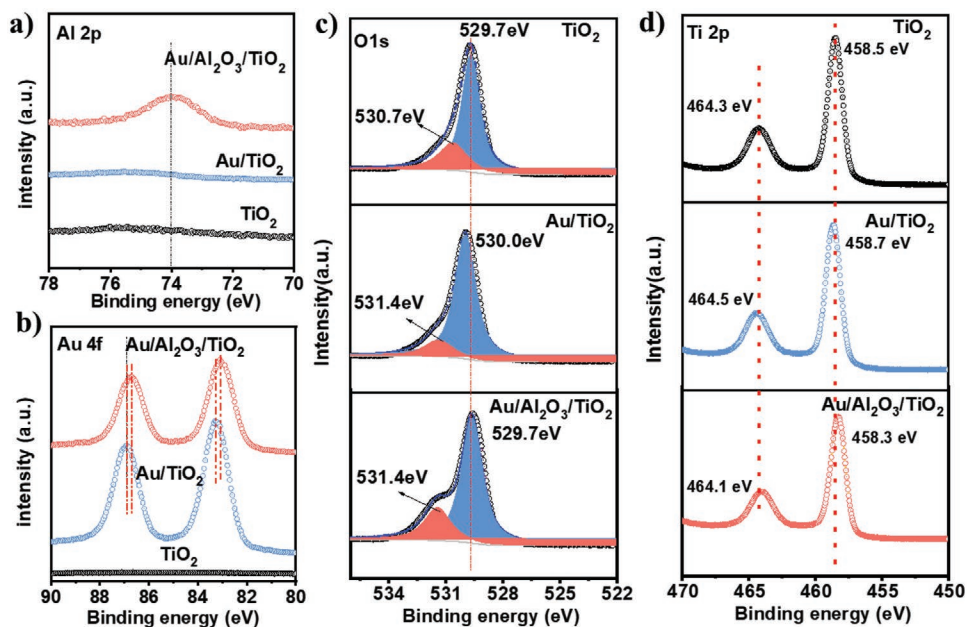


**Figure 5.** a) Al 2p XPS spectra of $TiO_2$, $Au/TiO_2$, and $Au/Al_2O_3/TiO_2$. b) Au 4f XPS spectra of $TiO_2$, $Au/TiO_2$, and $Au/Al_2O_3/TiO_2$. c) O 1s and d) Ti 2p XPS spectra of $TiO_2$, $Au/TiO_2$, and $Au/Al_2O_3/TiO_2$.

**ADVANCED**
**SCIENCE NEWS**
www.advancedsciencenews.com

**ADVANCED**
**FUNCTIONAL**
**MATERIALS**
www.afm-journal.de

interaction between Au and TiO$_2$ (Figure 5c). The Ti spectrum is composed of Ti 2p$_{3/2}$ at 458.5 eV and Ti 2p$_{1/2}$ peaks at 464.3 eV, indicating that Ti exists in the form of Ti$^{4+}$. The shift tendency of binding energy of Ti 2p among the three samples is similar to those of O 1s indicating the similar electron transfer process (Figure 5d). Thus, a strong electronic interaction is created via interfacial engineering to enhance interfacial contact. Additionally, the Schottky barrier height (SBH) is a crucial factor influencing the injection efficiency of hot electrons, which is determined by the work function of Au and the electron affinity of TiO$_2$. As the work function of Au remained unchanged, the electron affinity is related to the level of the valence band maximum (VBM); therefore, the VBM levels for both Au/TiO$_2$ and Au/Al$_2$O$_3$/TiO$_2$ were measured to estimate the effect of SBH. However, a comparable VBM level for both Au/TiO$_2$ and Au/Al$_2$O$_3$/TiO$_2$ strongly suggests that the SBH remained the same after introducing the Al$_2$O$_3$ layer, implying that the SBH is not the key factor for the different photocatalytic activities (Figure S9, Supporting Information).[41]

## 2.4. Interfacial Al$_2$O$_3$ for Improving Charge Separation

Ultrafast time-resolved spectra and surface photovoltage (SPV) spectra were recorded to further explore the role of Al$_2$O$_3$ in interfacial charge separation. As shown in **Figure 6**a, the relaxation dynamics of hot electrons for Au/TiO$_2$ and Au/Al$_2$O$_3$/TiO$_2$ can be well-fitted by three parameters: a fast component ($\tau_1$) within hundreds of femtoseconds and two slow components ($\tau_2$, $\tau_3$) at the order of picoseconds, the details of which are illustrated in **Table 1**. It was observed that the injection of hot electrons from Au to TiO$_2$ took place at sub-picoseconds in both Au/TiO$_2$ and Au/Al$_2$O$_3$/TiO$_2$, which is consistent with the results reported in the literature.[17,42] The transient absorption decay of hot electrons in the range 0.1–200 ps was due to the multiple charge recombinations of hot electrons with the holes in the Au nanoparticles. Clearly, the hot electrons of Au/Al$_2$O$_3$/TiO$_2$ exhibited prolonged lifetime compared with those of Au/TiO$_2$, indicating more efficient charge transfer. The above results were further validated by steady-state photovoltage characterization, as depicted in Figure 6b, in which the Au/Al$_2$O$_3$/TiO$_2$ shows a remarkably enhanced surface potential compared to Au/TiO$_2$ under light illumination ($\lambda = 550$ nm),

**Table 1.** Fitting parameters of carrier relaxation dynamics of Au/TiO$_2$ and Au/Al$_2$O$_3$/TiO$_2$.

| Sample | $\tau_1$ [ps] | $\tau_2$ [ps] | $\tau_3$ [ps] |
|---|---|---|---|
| Au/TiO$_2$ | 0.15 | 2.3 | 72.5 |
| Au/Al$_2$O$_3$/TiO$_2$ | 0.69 | 7.0 | 116.2 |

indicating that Au/Al$_2$O$_3$/TiO$_2$ exhibited a higher steady-state charge separation efficiency than Au/TiO$_2$, which is more likely correlated to the enhanced water oxidation performance. The spatial distribution of the hot carriers in Au/Al$_2$O$_3$/TiO$_2$ was acquired by Kelvin probe force microscopy (KPFM) to investigate whether the Al$_2$O$_3$ modification influenced the charge distribution (Figure S10, Supporting Information). The results indicate that hot holes generated via the SPR of Au nanoparticles in Au/Al$_2$O$_3$/TiO$_2$ mainly accumulated at the interface between Au and TiO$_2$, which is comparable with Au/TiO$_2$ in the previous work.[14] To conclude, the interfacial Al$_2$O$_3$ contacting Au and TiO$_2$ led to extended lifetime of hot carriers and higher steady charge separation efficiency, which contributed to the efficient plasmon-induced water oxidation on the Au/Al$_2$O$_3$/TiO$_2$ photocatalyst.

Theoretical simulation of the interfacial nanostructures of Au/Al$_2$O$_3$/TiO$_2$ was also employed (calculation details in Note S1, Supporting Information). A rutile TiO$_2$ (110) surface was used as the substrate, while three different adsorption sites were employed and compared for Au adsorption: on top of bridging O$_{2c}$ atoms, on top of bridging Ti$_{5c}$ atoms, and on top of bridging Ti$_{5c}$ and O$_{2c}$ atoms (Figure S11, Supporting Information). The bridging O$_{2c}$–Ti$_{5c}$ of the rutile TiO$_2$ (110) surface was the most stable adsorption site for Au atoms, because it possesses the lowest adsorption energy (Figure S12a,b, Supporting Information). After introducing Al$_2$O$_3$ species, the interface of Al$_2$O$_3$ and TiO$_2$ acted as a nucleation center to anchor Au particles and improve the binding energy of Au and TiO$_2$ (Figure S12c,d, Supporting Information). The results reveal that interfacial Au was prone to contacting both TiO$_2$ and Al$_2$O$_3$, with this structure possibly forming a strong Au–TiO$_2$ contact, which is in line with previous XPS results. Furthermore, in the Au/Al$_2$O$_3$/TiO$_2$ system, the interface state below $E_F$ was found to be formed by the hybridization of Au 5s and O 2p, while the interface state above the $E_F$ results from the
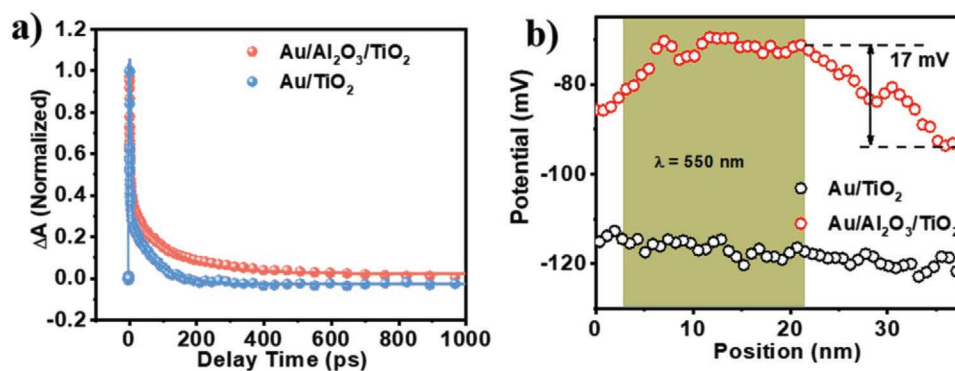


**Figure 6.** a) Ultrafast time-resolved spectra of Au/TiO$_2$ and Au/Al$_2$O$_3$/TiO$_2$. b) Surface photovoltage (SPV) of Au/TiO$_2$ and Au/Al$_2$O$_3$/TiO$_2$ under 550 nm illumination. SPV, light-illumination-induced surface potential change.

**ADVANCED
SCIENCE NEWS**

www.advancedsciencenews.com

**ADVANCED
FUNCTIONAL
MATERIALS**

www.afm-journal.de

electron transfer between the Au 5s and the Ti 3d orbitals (Figures S13 and S14, Supporting Information). As a result, the interfacial $Al_2O_3$ could promote the interaction between Au and $TiO_2$, which may explain the remarkable improvement in the interfacial charge separation and also possibly promote catalytic water oxidation at the interface between Au and $TiO_2$.

## 3. Conclusion

In summary, we took advantage of the interfacial modulation of $Al_2O_3$ to tune the extraction and separation of plasmonic hot carriers and obtain a high AQE of ≈1.3% at 520 nm for plasmon-induced water oxidation reactions in the Au/$TiO_2$ photocatalyst. The interfacial $Al_2O_3$ significantly improved the interaction between Au and $TiO_2$, and this interface structure greatly prolonged the lifetime of hot carriers and promoted the spatial separation of hot carriers in plasmonic photocatalysts. In contrast to the very fast interface charge transfer but short carrier lifetime in most plasmonic photocatalysts, we provide a strategy to realize long-lived hot carriers for potential applications in plasmonic photocatalysts. It is expected that our work may facilitate the understanding of the intrinsic roles of the interface structure in plasmonic photocatalysts for efficient solar energy conversion.

## 4. Experimental Section

*Photocatalyst Preparation*: Au/$TiO_2$ and Au/$Al_2O_3$/$TiO_2$ photocatalysts were prepared by a deposition–precipitation method. In brief, 1.0 g of rutile $TiO_2$ (anatase, P25) (Aladdin) was added to a 10.0 mL aqueous solution of $Al(NO_3)_3$ (Kemiou) containing 1% Al, the solution was stirred and heated at 353 K until it completely dried, and finally was annealed at various temperatures for 2 h. The as-prepared $Al_2O_3$/$TiO_2$ was added to a 0.42 M aqueous solution of urea (Sinopharm, AR). After vigorous stirring and sonication, 4.06 mL of 25 mM $HAuCl_4$ solution (Aladdin, 99.9%) was added to the suspension and maintained at 358 K under stirring for 4 h. The resulting samples were centrifuged, dried at 353 K, and post-heated at 673 K for 4 h to form Au/$Al_2O_3$/$TiO_2$. Similarly, Au/MgO ($Ga_2O_3$, ZnO, etc.)/$TiO_2$ was prepared by the same process. For comparison, Au/$TiO_2$ was synthesized via a similar process but without modification of the $Al_2O_3$ species.

The ALD deposition of $Al_2O_3$ was carried out by sequential exposure of trimethylaluminum (TMA) and water. For each ALD procedure, the reaction chamber temperature was set at 423 K, with a pulse time of 3 s, an exposure time of 40 s, and a nitrogen purge time of 180 s for TMA, and a pulse time of 30 s and a nitrogen purge time of 180 s for water. To avoid destroying the $Al_2O_3$ layer, Au nanoparticles were deposited onto the $TiO_2$ surface by an electrostatic adsorption process after annealing at 673 K for 1 h.[43] The Au nanoparticles were synthesized by adding a freshly prepared, ice-cold $NaBH_4$ solution (1.2 mL, 10 mM) to an 85 mL solution composed of $HAuCl_4$ (0.4 mL, 25 mM) and sodium citrate (14.7 mg), under vigorous stirring. $Al_2O_3$(NP)/$TiO_2$ was prepared by annealing a mixture of $TiO_2$ and $Al_2O_3$ nanoparticles (D&B 20 nm); then, Au nanoparticles were deposited onto $Al_2O_3$(NP)/$TiO_2$ by an electrostatic adsorption process to form Au/$Al_2O_3$ (NP)/$TiO_2$.

*Characterization*: Characterization by HRSEM was performed using a Hitachi S-5500 instrument with an operating voltage of 40 kV. HAADF images and compositional maps were performed using a JEM-ARM300F2 with an operating voltage of 300 kV. Powder XRD was conducted on a Rigaku D/Max-2500/PC powder diffractometer using Cu-K$\alpha$ radiation with an operating voltage of 40 kV and a current of 200 mA. The scanning range was 20–80° with a step scanning rate of 5° min$^{-1}$. UV–vis diffuse reflection spectra of the samples were obtained using a

UV–vis spectrophotometer (JASCO V-650) in the wavelength range of 200–900 nm. XPS measurements were carried out on a VG ESCALAB MK2 spectrometer with monochromatized Al-K$\alpha$ excitation and the C-1s peak (284.6 eV) used as the reference, arising from adventitious carbon. Electron paramagnetic resonance was recorded on a Bruker EPR A200 spectrometer at 110 K. The femtosecond transient absorption setup was based on a regenerative amplified Ti–sapphire laser system from Coherent (800 nm, 35 fs, 10 mJ pulse$^{-1}$, and 1 kHz repetition rate), nonlinear frequency-mixing techniques, and a Helios spectrometer (Ultrafast Systems LLC). Surface potential and SPV measurements were performed using an amplitude-modulated KPFM (Bruker Dimension V SPM system). The topography and surface potential of the samples were obtained through dual-scan processes, which effectively reduced the risk of cross-talk in the signals. A Pt/Ir coated-Si tip (SCM-PIT, Bruker) with a tip apex of 20 nm was used in the experiments, with a scanning rate of 0.5 Hz. The surface potential was defined as the difference between the work function of the tip and sample surface. For SPV measurements, monochromatic light were obtained from a Xe lamp (500 W, Beijing Perfectlight Co. Ltd) equipped with a double-prism monochromator (Zolix Omni-300) and a 350-nm bandpass filter.

*Theoretical Calculation*: All calculations were performed using the Vienna Ab Initio Simulation package. The density functional theory (DFT) calculations were carried out using GGA with the PBE exchange and correlation functional. The energy cutoff and convergence criteria used in this study were 400 eV, $10^{-4}$ eV, and 0.05 eV Å$^{-1}$ for the electronic and ionic loops, respectively. The k-points for structural optimization and density of states (DOS) analysis were 2 × 2 × 1 and 5 × 5 × 1, respectively. DFT + U calculations were performed for the DOS analysis, with a U parameter of the Ti atom set to 5 eV.

*Photocatalytic Water Oxidation Test*: Photocatalytic water oxidation was performed in a sealed system with a closed gas-circulation system and a GC test system. Briefly, 50 mg of the photocatalyst was added to 100 mL of ultrapure water in the presence of 5.0 mM $Fe(NO_3)_3$ as a sacrificial reagent. Before photoirradiation, the photoreactor was evacuated to remove air connected to the closed gas-circulation system. The light source was provided by a 300-W Xe arc lamp equipped with an optical cutoff filter (Y48, $\lambda \geq 480$ nm). A flow of cooling water was used to maintain the reaction mixture at room temperature. The evolved gases were analyzed by gas chromatography (Agilent; GC-7890A, MS-5A column, TCD, Ar carrier), equipped with a 5 Å molecular sieve column and a thermal conductivity detector (TCD).

*Photoelectrochemical Test*: In a typical synthesis, 30 mL of concentrated hydrochloric acid, 30 mL of deionized water, and 1.0 mL of titanium(IV) isopropoxide (Alfa) were mixed and transferred to a Teflon-lined stainless-steel autoclave. FTO substrates were then inserted in the autoclave, and the autoclave was maintained at 473 K for 20 min. Subsequently, an $Al_2O_3$ layer was introduced using ALD deposition for five cycles, then the Au nanoparticles were loaded by the deposition–precipitation method. PEC characterization was carried out using a typical three-electrode cell with a 300-W Xe lamp as the light source with a 480-nm cutoff filter, while a platinum plate and saturated calomel electrode were used as the counter electrode and reference electrode, respectively. For all PEC measurements, 0.5 M $NaSO_4$ (pH 6.6) was used as the electrolyte. Photocurrent–voltage potential curves were obtained using an electrochemical workstation (CHI 770d, CH Instruments, Inc.).

## Supporting Information

Supporting Information is available from the Wiley Online Library or from the author.

## Acknowledgements

## Conflict of Interest

The authors declare no conflict of interest.

## Keywords

[1] K. L. Kelly, E. Coronado, L. L. Zhao, G. C. Schatz, *J. Phys. Chem. B* **2003**, *107*, 668.

[2] H. A. Atwater, A. Polman, *Nat. Mater.* **2010**, *9*, 205.

[3] T. Tatsuma, H. Nishi, T. Ishida, *Chem. Sci.* **2017**, *8*, 3325.

[4] C. Zhan, X. Chen, J. Yi, J. Li, D. Wu, Z. Tian, *Nat. Rev. Chem.* **2018**, *2*, 216.

[5] Z. W. Seh, S. Liu, M. Low, S. Y. Zhang, Z. Liu, A. Mlayah, M. Y. Han, *Adv. Mater.* **2012**, *24*, 2310.

[6] J. Yang, Y. Guo, W. Lu, R. Jiang, J. Wang, *Adv. Mater.* **2018**, *30*, 1802227.

[7] P. Zhang, T. Wang, J. Gong, *Adv. Mater.* **2015**, *27*, 5328.

[8] W. Hou, S. B. Cronin, *Adv. Funct. Mater* **2013**, *23*, 1612.

[9] J. S. DuChene, B. C. Sweeny, A. C. Johnston-Peck, D. Su, E. A. Stach, W. D. Wei, *Angew. Chem., Int. Ed.* **2014**, *53*, 7887.

[10] C. Scales, P. Berini, *IEEE J. Quantum Electron* **2010**, *46*, 633.

[11] H. Chalabi, D. Schoen, M. L. Brongersma, *Nano Lett.* **2014**, *14*, 1374.

[12] G. Tagliabue, A. S. Jermyn, R. Sundararaman, A. J. Welch, J. S. DuChene, R. Pala, A. R. Davoyan, P. Narang, H. A. Atwater, *Nat. Commun.* **2018**, *9*, 3394.

[13] R. Negishi, S. I. Naya, H. Kobayashi, H. Tada, *Angew. Chem., Int. Ed.* **2017**, *56*, 10347.

[14] S. Wang, Y. Gao, S. Miao, T. Liu, L. Mu, R. Li, F. Fan, C. Li, *J. Am. Chem. Soc.* **2017**, *139*, 11771.

[15] S. Ye, C. Ding, M. Liu, A. Wang, Q. Huang, C. Li, *Adv. Mater.* **2019**, *31*, 1902069.

[16] S. Ye, C. Ding, R. Chen, F. Fan, P. Fu, H. Yin, X. Wang, Z. Wang, P. Du, C. Li, *J. Am. Chem. Soc.* **2018**, *140*, 3250.

[17] A. Furube, L. Du, K. Hara, R. Katoh, M. Tachiya, *J. Am. Chem. Soc.* **2007**, *129*, 14852.

[18] D. C. Ratchford, A. D. Dunkelberger, I. Vurgaftman, J. C. Owrutsky, P. E. Pehrsson, *Nano Lett.* **2017**, *17*, 6047.

[19] S. C. Warren, E. Thimsen, *Energy Environ. Sci.* **2012**, *5*, 5133.

[20] Q. Wei, S. Wu, Y. Sun, *Adv. Mater.* **2018**, *30*, 1802082.

[21] K. Wu, J. Chen, J. R. McBride, T. Lian, *Science* **2015**, *349*, 632.

[22] A. Tanaka, S. Sakaguchi, K. Hashimoto, H. Kominami, *ACS Catal.* **2013**, *3*, 79.

[23] L. Liu, P. Li, B. Adisak, S. Ouyang, N. Umezawa, J. Ye, R. Kodiyath, T. Tanabe, G. V. Ramesh, S. Ueda, H. Abe, *J. Mater. Chem. A* **2014**, *2*, 9875.

[24] S. Wang, B. Zeng, C. Li, *Chin. J. Catal.* **2018**, *39*, 1219.

[25] J. B. Priebe, J. Radnik, A. J. J. Lennox, M. M. Pohl, M. Karnahl, D. Hollmann, K. Grabow, U. Bentrup, H. Junge, M. Beller, A. Brückner, *ACS Catal.* **2015**, *5*, 2137.

[26] J. B. Priebe, M. Karnahl, H. Junge, M. Beller, D. Hollmann, A. Bruckner, *Angew. Chem., Int. Ed.* **2013**, *52*, 11420.

[27] Z. Bian, T. Tachikawa, P. Zhang, M. Fujitsuka, T. Majima, *J. Am. Chem. Soc.* **2014**, *136*, 458.

[28] P. Christopher, M. Moskovits, *Annu. Rev. Phys. Chem.* **2017**, *68*, 379.

[29] C. Li, D. Cahen, P. Wang, H. Li, J. Zhang, Y. Jin, *iScience* **2018**, *8*, 213.

[30] S. Tan, L. Liu, Y. Dai, J. Ren, J. Zhao, H. Petek, *J. Am. Chem. Soc.* **2017**, *139*, 6160.

[31] C. F. Bohren, D. R. Huffman, *Absorption and Scattering of Light by Small Particles*, Wiley, New York **1983**.

[32] Y. Miseki, K. Sayama, *RSC Adv.* **2014**, *4*, 8308.

[33] Y. Miseki, H. Kusama, H. Sugihara, K. Sayama, *J. Phys. Chem. Lett.* **2010**, *1*, 1196.

[34] C. Li, P. Wang, H. Li, M. Wang, J. Zhang, G. Qi, Y. Jin, *Nanoscale* **2018**, *10*, 14290.

[35] H. Li, S. Wang, F. Hong, Y. Gao, B. Zeng, R. Haider, F. Fan, J. Huang, C. Li, *J. Chem. Phys.* **2020**, *152*, 194702.

[36] R. Fang, Q. Sun, P. Zhou, W. Yang, P. Wang, D. Zhang, *Nanoscale Res. Lett.* **2013**, *8*, 92.

[37] L. Wang, H. Wang, A. E. Rice, W. Zhang, X. Li, M. Chen, X. Meng, J. P. Lewis, F. S. Xiao, *J. Phys. Chem. Lett.* **2015**, *6*, 2345.

[38] W. Zhan, Q. He, X. Liu, Y. Guo, Y. Wang, L. Wang, Y. Guo, A. Y. Borisevich, J. Zhang, G. Lu, S. Dai, *J. Am. Chem. Soc.* **2016**, *138*, 16130.

[39] S. Tsubota, T. Nakamura, K. Tanaka, M. Haruta, *Catal. Lett.* **1998**, *56*, 131.

[40] N. Roy, K. Bhunia, C. Terashima, A. Fujishima, D. Pradhan, *ACS Omega* **2017**, *2*, 1215.

[41] M. S. Arshad, S. Trafela, K. Z. Rozman, J. Kovac, P. Djinovic, A. Pintar, *J. Mater. Chem. C* **2017**, *5*, 10509.

[42] L. Du, A. Furube, K. Yamamoto, K. Hara, R. Katoh, M. Tachiya, *J. Phys. Chem. C* **2009**, *113*, 6454.

[43] P. Reineck, D. Brick, P. Mulvaney, U. Bach, *J. Phys. Chem. Lett.* **2016**, *7*, 4137.